Title
Development and Characterization of Modular Readout Design for Two-Panel Head-and-Neck Dedicated PET System Based on CZT Detectors.

Journal
IEEE Transactions on Radiation and Plasma Medical Sciences, 6(5)

ISSN
2469-7311

Authors
Wang, Yuli
Herbst, Ryan
Abbaszadeh, Shiva

Publication Date
2022-05-01

DOI
10.1109/trpms.2021.3111547

Peer reviewed

Published in final edited form as:

IEEE Trans Radiat Plasma Med Sci. 2022 May ; 6(5): 517–521. doi:10.1109/trpms.2021.3111547.

Development and Characterization of Modular Readout Design for Two-Panel Head-and-Neck Dedicated PET System Based on CZT Detectors

Yuli Wang [Student Member, IEEE],

Department of Electrical and Computer Engineering, University of California Santa Cruz, Santa Cruz, CA 95064, USA.

Ryan Herbst,

SLAC National Accelerator Labratory, 2575 Sand Hill Road, Menlo Park, CA, USA.

Shiva Abbaszadeh [Senior Member, IEEE]

Department of Electrical and Computer Engineering, University of California Santa Cruz, Santa Cruz, CA 95064, USA.

Abstract

Cadmium zinc telluride (CZT) detectors are suitable for various applications due to the good energy resolution and the simple pixilation to achieve high spatial resolution. Our group is developing a two-panel head and neck dedicated positron emission tomography system based on CZT detectors. Each panel will consist of 150 CZT crystals (4×4×0.5 cm^3) covering an area of 20×15 cm^2 in an edge-on configuration to achieve high detector efficiency at 511 keV. In this work, we present the design and development of a full data acquisition chain that enables a low noise and compact readout for each panel. The initial results of the readout circuit were quantified using a 1 kHz square wave test pulse. The pulse amplitude was chosen to generate approximately the same amount of charges as a 511 keV photon would provide in CZT. The best-case FWHM electronic noise at 511 keV was measured to be 0.69% ± 0.16% (3.52 ± 0.81 in keV units after conversion). The FWHM electronic noise at 511 keV for a complete DAQ chain was 4.33% ± 0.30% (22.13 ± 1.53 in keV units).

Keywords

Head and Neck; Positron Emission Tomography; Cadmium Zinc Telluride (CZT); Electronics Noise; Energy Resolution

I. Introduction

Many organ-dedicated molecular imaging systems have been developed since the introduction of positron emission tomography (PET) and single photon emission computed tomography (SPECT). A dedicated system could potentially result in better image quality due to the higher sensitivity achieved with close proximity to the organ of interest, reducing noncolinearity, utilizing detectors with better spatial resolution, and reducing the noise from other organs [1]. A dedicated system can be stand-alone such as dedicated brain systems [2]–[5] and dedicated breast systems [6]–[8] or it can be an add-on system such as using the

virtual pinhole approach [9]–[11] where a pinhole PET half-ring is inserted in a whole-body system. A dedicated system can be beneficial for head and neck cancer management as well. PET and positron emission tomography/computed tomography (PET/CT) are commonly used for head and neck cancer (HNC) diagnosing, staging, treatment planning, and assessing response to therapy [12]–[14].

In a simulation study, we demonstrated that a higher spatial resolution system can potentially improve the detection of tumor involvement in small lymph nodes (< 10 mm), and alleviate the challenges associated with identifying tumor boundaries in low spatial resolution PET where lesions appear “blurry” [15]. To minimize the amount of system in the line of sight of the patient for preventing claustrophobia, and to have the flexibility for imaging other organs and body parts that require high spatial resolution, a two-panel system configuration was proposed. The proposed system was considered an add-on system where it can be used immediately after the whole-body (WB) PET scan. The dedicated system will be moved into place for imaging while the patient is still on the bed of the WB PET/CT with no additional dose to the patient. A penalized maximum-likelihood (PML) image reconstruction method was developed to improve the limited-angle artifacts of the two-panel system utilizing the WB PET image as the prior image [16].

Two different detector technologies, cadmium zinc telluride (CZT) [17]–[19] and lutetium-yttrium oxyorthosilicate (LYSO) [20]–[22], with 1 mm and 2 mm pixellation and their measured energy resolution and time resolution were simulated [15]. It was shown that a two-panel system based on CZT could achieve better spatial resolution in 3D and higher accuracy in recovering the correct position of multiple interaction photon events (MIPEs) compared to the LYSO system. Although most brain PET scanners are using 2 mm crystal pixellation, 1 mm was chosen due to higher accuracy in recovering the correct position of MIPEs generated in CZT crystals [23], [24]. In CZT crystals with high energy resolution, better spatial resolution in 3D provides higher accuracy in recovering the true line of response in MIPEs [25].

In order to build a two-panel scanner with sufficient geometric efficiency for head and neck PET, each panel will consist of 150 CZT crystals ($4\times4\times0.5$ cm^3) covering an area of 20×15 cm^2 in an edge-on configuration to achieve high detector efficiency at 511 keV. CZT detectors for small animal PET imaging have been explored by several groups and commercial companies [26]–[28]. While a CZT detector with pixel-array configuration directly bump bonded to application-specific integrated circuit (ASIC) readout provides better energy resolution compared to a CZT detector with cross-strip configuration, an edge-on configuration of CZT crystals tightly stacked on top of each other could offer a high packing fraction (99%) and lower number of readout channels. As a consequence, the CZT detector design will remain similar to the previously developed cross-strip detector [29]. In this work we demonstrate a new full data acquisition (DAQ) chain for a prototype two-panel head and neck dedicated PET system, where each panel consists of 150 CZT detectors.

II. Materials and methods

The design of this unique system is based on challenges revealed from previous efforts to improve the count rates, time resolution, and noise floor of the full system [30], [31]. The cross-strip CZT crystal size ($4\times4\times0.5$ cm^3) and electrodes configuration with 39 anode strips (100 μm width and 1 mm pitch), 8 cathode strips (4900 μm width and 5 mm pitch) and 38 steering electrode strips (400 μm width) remained similar to previous design [28].

To incorporate large amounts of CZT detectors (300 CZT crystals for the whole two-panel system) and to achieve good system performance with the CZT detectors, we have proposed a modular readout electronics. This modular design has been developed to achieve a low noise floor by providing stable grounding and minimizing cross-talk between two RENA-3 ASICs. One panel diagram of the DAQ chain is shown in figure 1. It incorporates RENA boards (a total of 150 RENA boards for each panel in a full system), and 30:1 fan-in boards connecting the RENA boards to the PicoZed 7010/7020 board (a total of 5 fan-in boards for each panel in a full system). In each panel, 5:1 intermediate boards are used to provide high voltage bias to the CZT detectors. Each CZT detector is read out using two RENA-3 ASICs. Signal configurations (including clock signal, RST signal, sine signal (i.e. UV signal) and pulse signal) flow into the fan-in board through the external Ethernet cable which connects with an RJ-45 connector.

Data flow from the RENA board will fan-out via 1 GHz Ethernet cable connecting the small form-factor pluggable (SFP) connector and the White Rabbitor switch. The proper signal configuration is important to prevent the unwanted transfer of UV signal between ASIC readout channels. The UV signal originates from an external signal generator and is partitioned into two signals on the RENA board which are 90 degree out of phase sine waves (amplitude range 1–4V at 490 kHz). When a trigger event occurs, the sample and hold circuit of RENA ASIC captures the analog value on the UV signals. The digital sampling of the two sine waves provides unique points traversing around a circle that are used to identify the time at which sampling occurred. More details on the UV signals and crosstalk issue can be found in [30].

The RENA-3 board is capable of data transmission at 50 Mbps. PicoZed board 7010/7020 has the maximum 6.6 Gbps data transmission capability and is connected to a DAQ computer via fan-in board. Each fan-in board has a PicoZed board with the Xilinix ZYNQ XC7Z030 field programmable gate array (FPGA) and supports 30 RENA boards.

A. Design of the front-end circuits

The front-end circuit consists of the RENA boards and the intermediate boards. The RENA board was designed and extensively revised at the Molecular Imaging Instrumentation Laboratory (MIIL) at Stanford. It hosts a 100 pin Xilinx Spartan 3 FPGA and two RENA-3 ASICs. The Spartan 3 implements the readout protocol for both RENA-3 ASICs. The RENA board design remained similar to the previous design at MIIL with two modifications: i) removing the high voltage line and steering voltage line from the RENA board and ii) modifying the two RENA-3 ASICs channel configuration to improve the count rate. In previous design [30], anode 1 was read by RENA-3 ASIC 1 and anode 2 was readout by

RENA-3 ASIC 2 and so on (called alternative configuration). In the new design, RENA-3 ASIC 1 will readout anode channel 1 to anode channel 20 (half of the CZT crystal) and RENA-3 ASIC 2 will readout anode channel 21 to anode channel 39. A simulation study to demonstrate the difference between these two configurations can be found in [32]. This simulation study showed that the half-half configuration provides better load balancing between two RENA-3 ASICs and results in 2.82% higher per-channel readout-rate.

The intermediate board is designed to accommodate the half-half configuration, provide the high voltage (HV) bias of 150 V/mm to CZT crystals to reduce the charge drift time (compared to 100 V/mm in the previous design), and connect one array of 1×5 CZT crystals to five RENA boards.

B. Design of the back-end circuits: fan-in board

The fan-in board connects to a 1-column by 30-row array of RENA boards. The 6V DC power and ground from fan-in board are routed individually to each RENA board to avoid cross-talk between boards. In order to avoid logic metastability between subsystems in different clock domains, a single clock domain is enforced across the entire DAQ chain by the RJ-45 connector. The fan-in board is responsible for generating the system-wide 50 MHz clock, receiving RENA-3 ASIC timing signal (i.e. UV signal, U and V referred in the data sheet) from a function generator, and distributing the clock and UV signal to all 30 RENA boards attached to it. The fan-in board also provides the Xilinx JTAG chain interface for programming all 30 RENA boards. Lastly, the DAQ computer is connected to the detector system via fan-in board with the physical SFP connector.

C. Energy resolution characterization measurement with test pulse and point sources

To quantify the contribution of electronic noise of the designed circuits on the energy resolution and to estimate a lower bound for energy resolution, we used a square wave pulse as the excitation source for providing charge injection in each channel. The RENA-3 chip includes a 75 fF capacitor for charge injection in the amount of 75 fC/V. The square wave pulse frequency was 1 kHz with 250 mV peak-to-peak amplitude with no offset, which simulates approximately equivalent charge induced by a 511 keV photon in the CZT crystal (with electron-hole pair creation energy of around 5 eV). An example showing how different boards are connected together is presented in figure 2. Two fan-in boards are used to individually host 20 RENA boards (40 RENA boards in total). The corresponding intermediate boards and CZT detectors are used to make a completed DAQ chain. The whole system was packed into the light-tight Faraday cage during the experiments.

In our experiments, the data were collected through the following consecutive steps:

- 40 standalone RENA boards connected to the system (1880 channels in total)
- Intermediate boards connected to the RENA boards
- CZT detectors connected to the intermediate boards
- Turn on the HV bias of the CZT detectors
- Turn on the steering bias of the CZT detectors

- Turn on the UV signal

In order to get the standard deviation, this whole experiment was repeated 5 times. The spectral peak with full width at half maximum (FWHM) was calculated in both ADC and keV units.

The FWHM energy resolution was then measured by taking data from one CZT detector module (39 working anode channels) irradiated using a Ge-68 and Cs-137 point source. 10-minutes data acquisition time was set for both Ge-68 and Cs-137. The 511 keV peak from Ge-68 and 662 keV peak from Cs-137 were used for the channels calibration. No post data processing tools were used on the energy spectral (e.g. hole tailing correction). The spectral peak with FWHM was calculated in keV units.

III. Results

A. Measured energy resolution with standalone CZT detector

Figure 3 first shows the energy resolution (at 662 keV) results for 48 CZT crystals directly placed on a printed circuit board with cross-strip pattern for measurement. The maximum energy resolution and the minimum energy resolution of the 48 CZT detectors are 5% and 3%, FWHM at 662 keV, respectively. In the scale-up system, the edge-on cross strip CZT crystals are stacked on top of each other that precludes the possibility of coupling CZT crystals directly to the printed circuit board for readout. As a consequence, thin flexible circuits are utilized and bonded to CZT crystals to facilitate electrical contact between electrodes and RENA readout electronics. However, this approach will increase the trace length between the electrode and readout electronics. This approximately increases the input capacitance between 10 pF and 20 pF. As a consequence, we expect that the energy resolution degrades after bonding the CZT crystals to their flexible circuit. However, from the previous experience [30] this degradation will remain within less than 1%.

B. Measurements results with test pulse for electronic noise

The results of measured electronic noise with different circuit conditions are summarized in table I. When using square wave as the excitation signal and only the RENA boards were connected to the back-end readout system (case 1), the FWHM was 5.60 ± 1.31 in ADC units or 3.52 ± 0.81 in keV units. When the intermediate boards were connected to the RENA boards (case 2), FWHM broadened to 15.00 ± 1.79 in ADC units or 9.35 ± 1.12 in keV units. The CZT detector was then connected to the intermediate board (case 3), further broadening the FWHM value of spectral peak to 18.10 ± 1.47 in ADC units or 11.34 ± 0.92 in keV units. The FWHM values of the spectral peak were measured after the application of high voltage bias (case 4) and steering voltage bias (case 5), which came to 25.70 ± 3.51 in ADC units or 15.89 ± 2.20 in keV units and 28.50 ± 4.23 in ADC units or 17.62 ± 2.65 in keV units, respectively. The final step was to apply the UV signal (case 6) and the FWHM value of spectral peak went to 35.35 ± 2.44 in ADC units or 22.13 ± 1.53 in keV units. The spread of the energy resolution in each case for 3 CZT crystals with 117 channels are plotted in histograms shown in figure 4 (a)-(f).

C. Measurements results for energy resolution with point source

The spread of the energy resolution for 3 CZT crystals with 117 channels for Ge-68 and Cs-137 are plotted in histograms shown in figure 4 (g)-(h). The average FWHM values of Ge-68 and Cs-137 were 8.08% at 511 keV and 7.81 % at 662 keV, respectively. Examples of one channel spectral peak for Ge-68 and one channel spectral peak for Cs-137 are shown in figure 12 (i) and (j), respectively. The noise floor of the system is low and the lowest threshold of keV of the new system resides between 10 keV to 50 keV.

IV. Discussion

A. Requirement of a low noise readout system for PET using CZT

Over the past 10 years (from 2010 to 2020), the cost of CZT detectors per/cm^3 has been reduced tremendously (almost 10 fold), leading to the rapid adoption of CZT by multinational original equipment manufacturers (OEMs), such as the SPECT cameras introduced by GE Healthcare. There has been a significant improvement and breakthrough in CZT crystal growth technology, both performance and yield, leading to a significant cost reduction of CZT detectors compared to previous high performance CZT produced by the low yield high-pressure Bridgman method. The introduction of the Traveling Heather Method (THM) of CZT crystal growth in particular, was a game changer since this technology not only increases the single crystal yield but also improves the uniformity of the material significantly [33]. Despite that the current price of CZT detectors is still higher than that of scintillators, the rapid price reduction trend of CZT is expected to continue. As a consequence, there is a need for low-noise readout electronics to support reading out a large volume of CZT crystals. The goal is to maintain the overall FWHM of the system to be defined by the energy resolution of the CZT detectors. A low noise system enables triggering of the channels at lower energy. In order to detect MIPEs accurately, a low noise system capable of a low energy threshold per interaction is desired [23]. In addition, the system FWHM will be quadrature sum of the FWHM values for the detectors and the system noise. The energy resolution of the purchased cross-strip CZT crystals before bonding to flexible circuit are within 3–5 % FWHM at 662 keV. The average energy resolution of one CZT crystal (with 4% energy resolution at 662 keV measured at Kromek before bonding) after bonding to a flexible circuit was measured utilizing the scale-up electronics. The measured energy resolution (7.81% at 662 keV) without any hole tailing correction is in good agreement with the quadrature sum of the FWHM value of the CZT crystal and system noise. Based on previous effort for hole tailing correction, we expect to improve the energy resolution from 7.81% at 662 keV to 6% [17].

B. Comparison of the system electronic noise performance

Building on previous experience on the development of a DAQ system for small animal PET system based on a similar CZT detector design [30], [34], [35], we have improved the readout electronic noise in a new design for a two-panel head-and-neck PET system. The comparison of the electronic noise among three iteration systems is shown in figure 5. The electronic noise of the small animal system [34] and the revised small animal system [30] at 511 keV using the square test pulse were measured to be around 6.5% FWHM and 5% FWHM, respectively. The major improvement from the initial system [34] to the revised

system [30] was adding filtering to remove the noise contribution due to HV. We have further improved our new system to accommodate better fanning out of the HV path. In the previous design, the HV/steering voltage bias fanned out from the fan-in board to the RENA boards and then to the intermediate boards. In the current design, the HV/steering voltages fan out directly to the intermediate boards. We have also changed the RENA-3 ASICs channel configuration (from alternate to half-half configuration), improved the layout of the intermediate boards, and developed a new fan-in board that directly connects to RENA boards without using a fragile flexible circuit to reduce crosstalk and noise. The electronic noise and cross-talk have been significantly reduced in the new system. The lowest threshold of keV of the new system resides between 10 keV to 50 keV compared to 100 keV to 200 keV in the previous system [28]. The lower threshold of the system will allow detecting scatter events with lower energy in CZT detector and more accurate Compton recovery. The electronic noise of the new system was reduced to around 4% FWHM at 511 keV using the test pulse. In addition, the new system is capable of working at higher CZT biasing voltage (up to 1000V) compared to the previous design (up to 600V).

V. Conclusions

Modular readout electronics consisting of intermediate boards to support an array of (1 by 5) RENA boards and fan-in boards to support an array of (1 by 30) RENA boards were designed. By scaling up these boards, a full data acquisition chain can be constructed for the two-panel PET system based on cross-strip CZT detectors. A stable test pulse (a 1 kHz square wave pulse frequency with 250 mV peak-to-peak amplitude with no offset) was used to determine the noise level of this design by connecting 40 RENA boards (1880 readout channels in total) to two fan-in boards. The electronic noise contribution to FWHM was 3.52 ± 0.81 in keV units at best case (RENA boards only). The electronic noise contribution to FWHM was 22.13 ± 1.53 in keV units (4.33% ± 0.30%) for a complete DAQ chain. The electronic noise performance of our readout circuits improved by removing the flexible circuits from RENA boards, connecting RENA boards directly to fan-in boards, removing the HV bias from fan-in boards and RENA boards, and applying the HV directly to intermediate boards. These modifications led to an improvement to statistical fluctuation due to electronic noise and an improvement to the readout energy resolution compared to previous designs (improvement of approximately 2% FWHM at 511 keV). Future work includes integrating the bonded CZT detectors in each panel, and testing the system-wide energy resolution.

Acknowledgment

The authors acknowledge the support from the National Institute of Biomedical Imaging and Bioengineering of the National Institutes of Health under Award Number R01EB028091.

References

[1]. González AJ, Snchez F, and Benlloch J, “Organ-dedicated molecular imaging systems,” IEEE Transactions on Radiation and Plasma Medical Sciences, vol. 2, no. 5, pp. 388–403, 2018.

[2]. González A, Gonzalez-Montoro A, Vidal L, Barbera J, Aussen-hofer S, Hernandez L, Moliner L, Sanchez F, Correcher C, Pincay E, and Cañizares G, “Initial results of the MINDView PET insert

inside the 3T mMR," IEEE Transactions on Radiation and Plasma Medical Sciences, vol. 3, no. 3, pp. 343–351, 2019.

[3]. Yamamoto S, Honda M, Oohashi T, Shimizu K, and Senda M, "Development of a brain pet system, PET-Hat: a wearable PET system for brain research," IEEE Transactions on Nuclear Science, vol. 58, no. 3, pp. 688–673, 2011.

[4]. Wang Z, Yu W, and Xie S, "A dedicated PET system for human brain and head/neck imaging," in 2013 IEEE Nuclear Science Symposium and Medical Imaging Conference (2013 NSS/MIC). IEEE, 2013, pp. 1–4.

[5]. Melroy S, Bauer C, McHugh M, Carden G, Stolin A, Majewski S, Brefczynski-Lewis J, and Wuest T, "Development and design of next-generation head-mounted ambulatory microdose positron-emission tomography (AM-PET) system," Sensors, vol. 17, no. 5, p. 1164, 2017. [PubMed: 28534848]

[6]. Hsu DF, Freese DL, Reynolds PD, Innes DR, and Levin CS, "Design and performance of a 1 mm 3 resolution clinical pet system comprising 3-d position sensitive scintillation detectors," IEEE Transactions on Medical Imaging, vol. 37, no. 4, pp. 1058–1066, 2018. [PubMed: 29621003]

[7]. Weinberg IN, Beylin D, Zavarzin V, Yarnall S, Stepanov PY, Anashkin E, Narayanan D, Dolinsky S, Lauckner K, and Adler LP, "Positron emission mammography: high-resolution biochemical breast imaging," Technology in cancer research & treatment, vol. 4, no. 1, pp. 55–60, 2005. [PubMed: 15649088]

[8]. Moliner L, Gonzalez A, Soriano A, Sanchez F, Correcher C, Orero A, Carles M, Vidal L, Barbera J, Caballero L. et al. , "Design and evaluation of the MAMMI dedicated breast PET," Medical physics, vol. 39, no. 9, pp. 5393–5404, 2012. [PubMed: 22957607]

[9]. Tai Y-C, Wu H, Pal D, and O'Sullivan JA, "Virtual-pinhole PET," Journal of Nuclear Medicine, vol. 49, no. 3, pp. 471–479, 2008. [PubMed: 18287272]

[10]. Mathews AJ, Komarov S, Wu H, O'Sullivan JA, and Tai Y-C, "Improving PET imaging for breast cancer using virtual pinhole PET half-ring insert," Physics in Medicine & Biology, vol. 58, no. 18, p. 6407, 2013. [PubMed: 23999026]

[11]. Jiang J, Li K, Wang Q, Puterbaugh K, Young JW, Siegel SB, O'Sullivan JA, and Tai Y-C, "A second-generation virtual-pinhole PET device for enhancing contrast recovery and improving lesion detectability of a whole-body PET/CT scanner," Medical physics, vol. 46, no. 9, pp. 4165–4176, 2019. [PubMed: 31315157]

[12]. Yu H, Caldwell C, Mah K, and Mozeg D, "Coregistered FDG PET/CT-based textural characterization of head and neck cancer for radiation treatment planning," IEEE transactions on medical imaging, vol. 28, no. 3, pp. 374–383, 2008.

[13]. Al-Ibraheem A, Buck A, Krause BJ, Scheidhauer K, and Schwaiger M, "Clinical applications of FDG PET and PET/CT in head and neck cancer," Journal of oncology, vol. 2009, 2009.

[14]. Hustinx R. and Lucignani G, "Pet/ct in head and neck cancer: an update," European journal of nuclear medicine and molecular imaging, vol. 37, no. 3, pp. 645–651, 2010. [PubMed: 20187296]

[15]. Li M, Yockey B, and Abbaszadeh S, "Design study of a dedicated head and neck cancer PET system," IEEE transactions on radiation and plasma medical sciences, vol. 4, no. 4, pp. 489–497, 2020. [PubMed: 32632397]

[16]. Zhang H, Wang Y, Qi J, and Abbaszadeh S, "Penalized maximum-likelihood reconstruction for improving limited-angle artifacts in a dedicated head and neck PET system," Physics in Medicine & Biology, 2020.

[17]. Abbaszadeh S, Gu Y, Sikora U, and Levin CS, "First acquisition of data from a prototype 3-d position sensitive CZT PET system," in 2014 IEEE Nuclear Science Symposium and Medical Imaging Conference (NSS/MIC). IEEE, 2014, pp. 1–2.

[18]. Wang Y, Li Y, Yi F, Li J, Xie S, Peng Q, and Xu J, "Two-crossed-polarizers based optical property modulation method for ionizing radiation detection for positron emission tomography," Physics in Medicine & Biology, vol. 64, no. 13, p. 135017, 2019.

[19]. Wang Y, Tao L, Abbaszadeh S, and Levin C, "Further investigations of a radiation detector based on ionization-induced modulation of optical polarization," Physics in Medicine & Biology, vol. 66, no. 5, p. 055013, 2021.

[20]. Li M. and Abbaszadeh S, “Depth-of-interaction study of a dual-readout detector based on tofpet2 application-specific integrated circuit,” Physics in Medicine & Biology, vol. 64, no. 17, p. 175008, 2019.

[21]. Li M, Wang Y, and Abbaszadeh S, “Development and initial characterization of a high-resolution pet detector module with doi,” Biomedical Physics & Engineering Express, vol. 6, no. 6, p. 065020, 2020.

[22]. Romanchek G, Wang Y, Marupudi H, and Abbaszadeh S, “Performance of optical coupling materials in scintillation detectors post temperature exposure,” Sensors, vol. 20, no. 21, p. 6092, 2020. [PubMed: 33120896]

[23]. Abbaszadeh S, Chinn G, and Levin CS, “Positioning true coincidences that undergo inter-and intra-crystal scatter for a sub-mm resolution cadmium zinc telluride-based pet system,” Physics in Medicine & Biology, vol. 63, no. 2, p. 025012, 2018.

[24]. Farahmandzadeh M. and Abbaszadeh S, “A machine learning approach for identifying correct sequence of multiple photon interaction event in pet systems,” Journal of Nuclear Medicine, vol. 61, no. supplement 1, pp. 1514–1514, 2020. [PubMed: 32169912]

[25]. Yang S, Li M, Reed M, Hugg J, Chen H, and Abbaszadeh S, “Effect of CZT system characteristics on compton scatter event recovery,” IEEE Transactions on Radiation and Plasma Medical Sciences, vol. 4, no. 1, pp. 91–97, 2019. [PubMed: 31922083]

[26]. Drezet A, Monnet O, Montemont G, Rustique J, Sanchez G, and´ L. Verger, “CdZnTe detectors for the positron emission tomographic imaging of small animals,” in IEEE Symposium Conference Record Nuclear Science 2004., vol. 7. IEEE, 2004, pp. 4564–4568.

[27]. Vaska P, Dragone A, Lee W, Kim D-H, Pratte J-F, Cui Y-G, Fried J, Krishnamoorthy S, Bolotnikov A, Park S-J et al., “A prototype CZT-based PET scanner for high resolution mouse brain imaging,” in 2007 IEEE Nuclear Science Symposium Conference Record, vol. 5. IEEE, 2007, pp. 3816–3819.

[28]. Abbaszadeh S. and Levin CS, “New-generation small animal positron emission tomography system for molecular imaging,” Journal of Medical Imaging, vol. 4, no. 1, p. 011008, 2017.

[29]. Gu Y. and Levin C, “Study of electrode pattern design for a czt-based pet detector,” Physics in Medicine & Biology, vol. 59, no. 11, p. 2599, 2014. [PubMed: 24786208]

[30]. Abbaszadeh S, Gu Y, Reynolds PD, and Levin CS, “Characterization of a sub-assembly of 3d position sensitive cadmium zinc telluride detectors and electronics from a sub-millimeter resolution PET system,” Physics in Medicine & Biology, vol. 61, no. 18, p. 6733, 2016. [PubMed: 27551981]

[31]. Wang Y, Herbst R, and Abbaszadeh S, “Back-end readout electronic design and initial results: a head-and-neck dedicated PET system based on CZT,” in Medical Imaging 2021: Physics of Medical Imaging, vol. 11595. International Society for Optics and Photonics, 2021, p. 1159510.

[32]. Li M. and Abbaszadeh S, “Influence of channel configuration on bandwidth of cadmium zinc telluride detector with a cross-strip pattern,” Radiation Physics and Chemistry, vol. 155, pp. 213–216, 2019.

[33]. Chen H, Li H, Reed MD, Sundaram AG, Eger J, Hugg JW, Abbaszadeh S, Li M, Montemont G, Verger L. et al., “Development of large-volume high-performance monolithic CZT radiation detector,” in Hard X-Ray, Gamma-Ray, and Neutron Detector Physics XX, vol. 10762. International Society for Optics and Photonics, 2018, p. 107620N.

[34]. Gu Y, “High-resolution small animal positron emission tomography system based on 3-d position-sensitive cadmium zinc telluride photon detectors,” Ph.D. dissertation, Stanford University, 2014.

[35]. Wang Y, Herbst R, and Abbaszadeh S, “Electronic noise characterization of a dedicated head-and-neck cancer PET based on CZT,” vol. 62, no. 1154. Soc Nuclear Med, 2021.

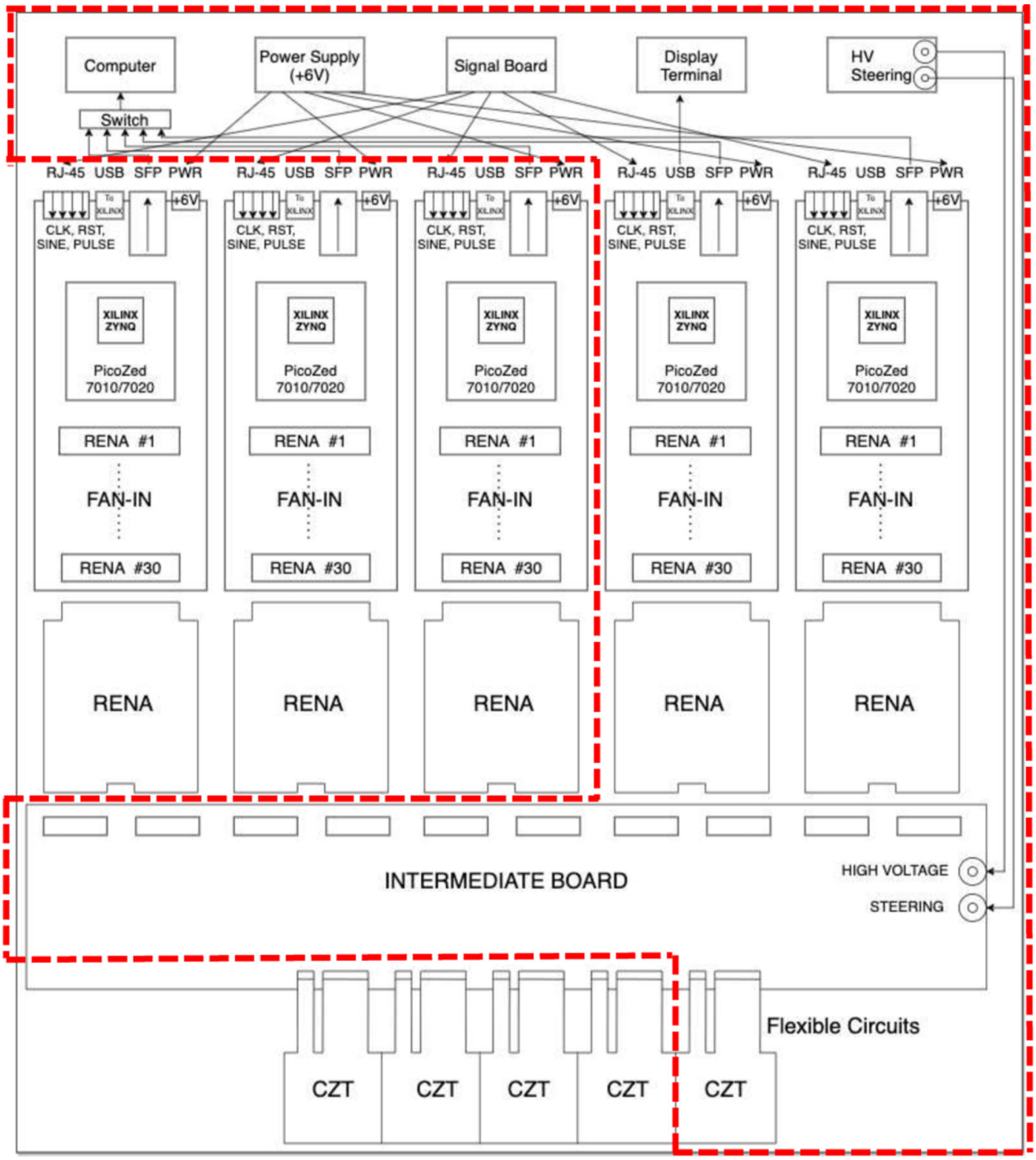

Fig. 1.

Architecture of the DAQ chain of one panel for the head and neck PET system. For quantifying the level of electronic noise, the measurement was completed with the red dashed box hardware electronics. The detailed measurement method and results will be presents in section II-C and section III, including 2 fan-in boards, 2 PicoZed boards, 40 RENA boards, 1 intermediate board and 1 CZT detector module and other external electronics.

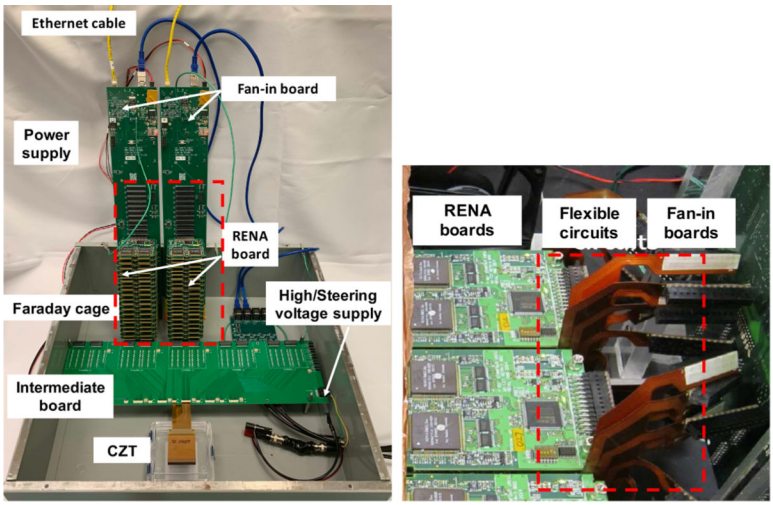

Fig. 2.

(a) An example picture of the experimental setup used for the measurement with test pulse. It consists of 2 fan-in boards, 40 RENA boards, intermediate board and CZT detector. The direct connection between the RENA board and the fan-in board is marked with red dashed box. (b) An example picture of previous system [30]. The RENA boards are connected to the fan-in boards through the red dashed box marked flexible circuit.

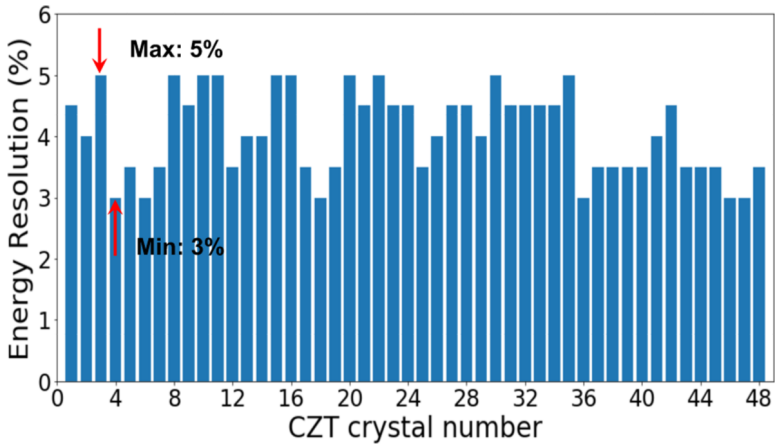

Fig. 3.

Summary of the average energy resolution of 39 anode channels for 48 CZT crystals at 662 keV before bonding to flexible circuit measured at Kromek utilizing a comb-tooth finger probe for direct contact with cross-strip electrodes and using Cs-137 point source.

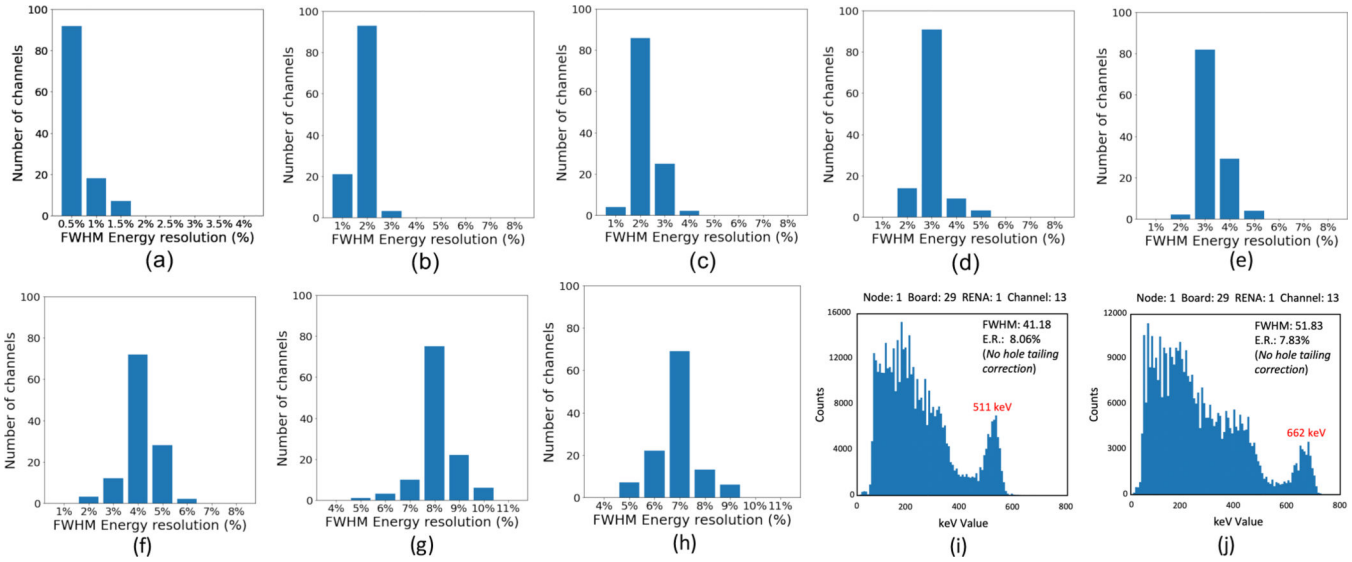

Fig. 4.

Histograms showing the spread of the energy resolution for all channels (117 channels) from three available CZT detectors for each case. (a) case 1 with only RENA boards; (b) case 2 with the addition of intermediate board; (c) case 3 with the addition of CZT detector; (d) case 4 with additional application of high voltage bias; (e) case 5 with additional application of steering voltage bias; (f) case 6 with additional application of UV signal; (g) case 6 with additional application of Ge-68 point source; (h) case 6 with additional application of Cs-137 point source; (i) Energy calibrated spectra for Ge-68. (j) Energy calibrated spectra for Cs-137. No hole correction was applied, yielding a lower than expected energy resolution.

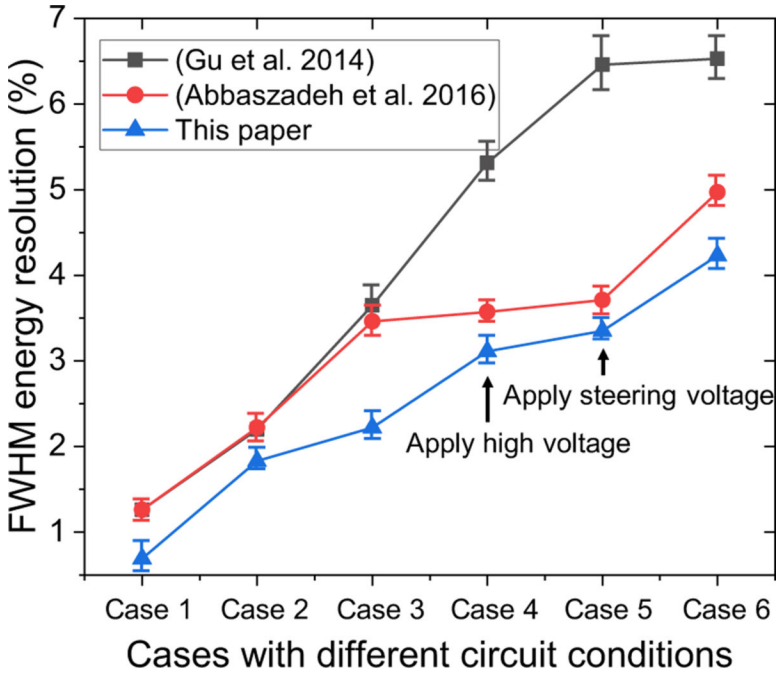

Fig. 5.

Comparison of electronic noise performance among the small animal system of [34], the small animal system of [30] and the system of this paper at each different case. Two arrows indicate the case of applying HV and the case of applying steering bias voltage, which are two major noise sources of the system.

TABLE I

SUMMARY OF THE QUANTIFIED ELECTRONIC NOISE CONTRIBUTION AT DIFFERENT CIRCUIT CONDITIONS UTILIZING A TEST PULSE GENERATING THE SAME AMOUNT OF CHARGES (AS A 511 KEV PHOTON GENERATE IN CZT) TO DEMONSTRATE THE BEST CASE FWHM ENERGY RESOLUTION AT 511 KEV.

No.	Circuit conditions	Noise source	Approximate Value	FWHM Energy Resolution
Case 1	Standalone RENA boards	Best Case	150–280 eRMS for RENA ASIC	0.69% ± 0.16%
Case 2	Intermediate boards	Capacitance	50 pF	1.83% ± 0.22%
Case 3	CZT detector	Capacitance	32 pF	2.22% ± 0.18%
Case 4	High voltage (−750 V)	i_{dark} (Cathode)	125 nA	3.11% ± 0.43%
Case 5	Steering voltage (−80V)	i_{dark} (Steering)	375 nA	3.45% ± 0.52%
Case 6	UV signal (1.6Vpp)	Cross-talk	—	4.33% ± 0.30%